BBA - Proteins and Proteomics 1870 (2022) 140772

Contents lists available at ScienceDirect

BBA - Proteins and Proteomics

journal homepage: www.elsevier.com/locate/bbapap

Silybins inhibit human IAPP amyloid growth and toxicity through stereospecific interactions

Sara García-Viñuales [a,1], Ioana M. Ilie [b,1], Anna Maria Santoro [a], Valeria Romanucci [c], Armando Zarrelli [c], Giovanni Di Fabio [c], Amedeo Caflisch [b,*], Danilo Milardi [a,*]

[a] Consiglio Nazionale delle Ricerche, Istituto di Cristallografia, Sede Secondaria di Catania, Via Paolo Gaifami 18, 95126 Catania, Italy
[b] Department of Biochemistry, University of Ziirich, Ziirich CH-8057, Switzerland
[c] Department of Chemical Sciences, University of Naples Federico II, Via Cintia 4, I-80126 Napoli, Italy

ARTICLE INFO

Keywords:
Molecular dynamics
Diabetes
Aggregation
Peptide
Inhibitors

ABSTRACT

Type 2 Diabetes is a major public health threat, and its prevalence is increasing worldwide. The abnormal accumulation of islet amyloid polypeptide (IAPP) in pancreatic β-cells is associated with the onset of the disease. Therefore, the design of small molecules able to inhibit IAPP aggregation represents a promising strategy in the development of new therapies. Here we employ *in vitro*, biophysical, and computational methods to inspect the ability of Silybin A and Silybin B, two natural diastereoisomers extracted from milk thistle, to interfere with the toxic self-assembly of human IAPP (hIAPP). We show that Silybin B inhibits amyloid aggregation and protects INS-1 cells from hIAPP toxicity more than Silybin A. Molecular dynamics simulations revealed that the higher efficiency of Silybin B is ascribable to its interactions with precise hIAPP regions that are notoriously involved in hIAPP self-assembly *i.e.,* the S20-S29 amyloidogenic core, H18, the N-terminal domain, and N35. These results highlight the importance of stereospecific ligand-peptide interactions in regulating amyloid aggregation and provide a blueprint for future studies aimed at designing Silybin derivatives with enhanced drug-like properties.

1. Introduction

Diabetes mellitus is a metabolic disorder characterized by abnormal blood glucose levels and increased risk of damage to the nerves, kidneys, and cardiovascular system. Different types of diabetes include i) type 1 diabetes (T1D), ii) type 2 diabetes (T2D), and iii) gestational diabetes [1]. T1D, an autoimmune disease that leads to progressive loss of pancreatic β-cells, represents nearly 10% of diabetes cases [2,3]. T2D, the most common form with 85% of all diabetes cases, is associated with aging, a sedentary lifestyle and obesity. The global prevalence of T2D is dramatically increasing and the total number of patients is expected to rise to 700 million within the next 15 years [4]. T2D diabetes or 'non-insulin-dependent diabetes mellitus' (NIDDM), being associated with an abnormal accumulation of islet amyloid polypeptide (IAPP) in pancreatic β-cells, belongs to the family of protein conformational disorders (PCDs) [5,6].

The human islet amyloid polypeptide (hIAPP or amylin) is a 37 residues peptide with a disulfide bridge linking the two cysteines C2 and C7, required for its full biological activity (Fig. 1a) [7]. hIAPP exhibits a high propensity to aggregate into amyloid fibrils both *in vitro* and *in vivo* [8] and its aggregates are toxic to β-cells [9,10]. hIAPP is an intrinsically disordered protein (IDP) and is known to adapt its secondary structure in response to the environment. Thereby, it is mainly disordered in solution, but it can curl into compact helix-coil structures or short-lived α-helices, and can also form antiparallel β-sheets and β-hairpins [11,12]. Each domain of IAPP modulates amylin self-assembly. The N-terminus, comprising the first 20 residues, is involved in peptide interactions with lipid membranes [13,14]. The segment A13-H18 was shown to modulate IAPP amyloid formation in aqueous solution [15]. The S20-S29 domain or the "amyloid core" represents the building block of amyloid accumulations and modifications in this region can relinquish the aggregation efficiency of amylin. For instance, rat IAPP (rIAPP), which differs from hIAPP in five residues in the amyloid core, has a reduced ability to form amyloid fibrils [16,17]. Furthermore, peptides cleaved from the C-terminal domain T30-Y37 can interfere with amyloid formation [18].

* Corresponding authors.
E-mail addresses: caflisch@bioc.uzh.ch (A. Caflisch), danilo.milardi@cnr.it (D. Milardi).
[1] These authors equally contributed to this work.

https://doi.org/10.1016/j.bbapap.2022.140772
Received 7 February 2022; Received in revised form 9 March 2022; Accepted 13 March 2022
Available online 17 March 2022

The identification of specific chemotypes able to inhibit the toxic accumulation of hIAPP is considered a promising strategy to counteract β-cells loss in diabetic patients. Most of these molecules are characterized by multiple aromatic rings (*e.g.* polyphenols) and include tanshinone I and IIA [19], genistein [19], heparin fragments [20], naproxen analogues [21], lipoic and ascorbic acid [22], epigallocatechin gallate (EGCG) [23], resveratrol [24] and diazenyl-derivatives of pyridazinylpyrazolone [25]. Several studies reported that silibinin, the main component of a milk thistle extract named silymarin [26,27], may regulate glucose release in blood [28], and inhibit hIAPP aggregation [29,30]. However, the molecular mechanisms responsible for the protective effects of silibinin remain to be understood.

Silibinin is a (1:1) mixture of silybin A (Sil A) and silybin B (Sil B), two flavonolignan diastereoisomers [31] (Fig. 1). Silybins are molecules with alternate benzenic rings and O-heterocycles; their chemical structure is composed of two main groups, the flavonol group taxifolin and the phenylpropanoid group coniferyl alcohol, which are linked through an oxeran ring [32] (Fig. 1b). Sil A and Sil B are trans-diastereoisomers with different configurations of their stereocenters C-7″ and C-8″ (7″R, 8″R in Sil A and 7″S, 8″S in Sil B) and the same configuration in the other two stereogenic centers (2R,3R in both cases) (Fig. 1c and d). They contain five hydroxyl groups, out of which three are phenolic (5-OH, 7-OH, and 4′-OH) with pK_a values of around 6.6, 7.7–7.9, and 11.0, respectively [33]. The oxo group in position 4 is conjugated with the adjacent aromatic ring and may interact, depending on pH, with 5-OH through a hydrogen bond, acting as a free electron-pair donor.

In this work we investigate the effects of each of the two diastereoisomers of silibinin *in vitro* and by atomistic simulations. We perform cell viability assays on rat insulinoma INS-1 cells to determine which of the two diastereomers is more protective against the proteotoxic stress of hIAPP aggregates. We then run biophysical experiments to find out whether the cytoprotective activity of silybins is related to their ability to inhibit hIAPP aggregation. In parallel, we perform molecular dynamics (MD) simulations to unveil the molecular mechanisms driving cytoprotective hIAPP/silybins interactions.

2. Results

2.1. Sil B attenuates hIAPP toxicity and aggregation propensity

Silibinin is known to reduce hIAPP-induced toxicity in cultured rat insulinoma INS-1 cells [30]. However, it is unknown which of the two silibinin components, *i.e.* Sil A or Sil B, has the higher cytoprotective effect. Thus, we performed tetrazolium salt (3-(4,5-dimethylthiazol-2-yl)-2,5- diphenyltetrazolium bromide) reduction (MTT) assays [34,35] to compare the effects of Sil A and Sil B on INPS-1 cells viability after 24 h treatment with 5 μM hIAPP. We found that in these experimental conditions hIAPP reduces cell viability by about 20% (Fig. 2a). Cell viability experiments (Fig. 2a) showed for both diastereoisomers a dose-dependent mitigation of hIAPP toxicity. Albeit at peptide/ligand (P/L) molar ratio 1:1 (*i.e.*, 5 μM) only a partial recovery was observed, at higher concentrations (10–15 μM), Sil B fully rescued hIAPP cytotoxicity. Moreover, Sil B exhibits a significantly more protective effect respect to Sil A at all ligand concentrations.

Although these results are in line with the antioxidant properties of the two ligands (see Fig. S1), to probe the relationship between the anti-aggregating effects and cytoprotective properties of silybins, we performed ThT assays at 1:0.1, 1:0.4, and 1:0.8 peptide/ligand (P/L) molar

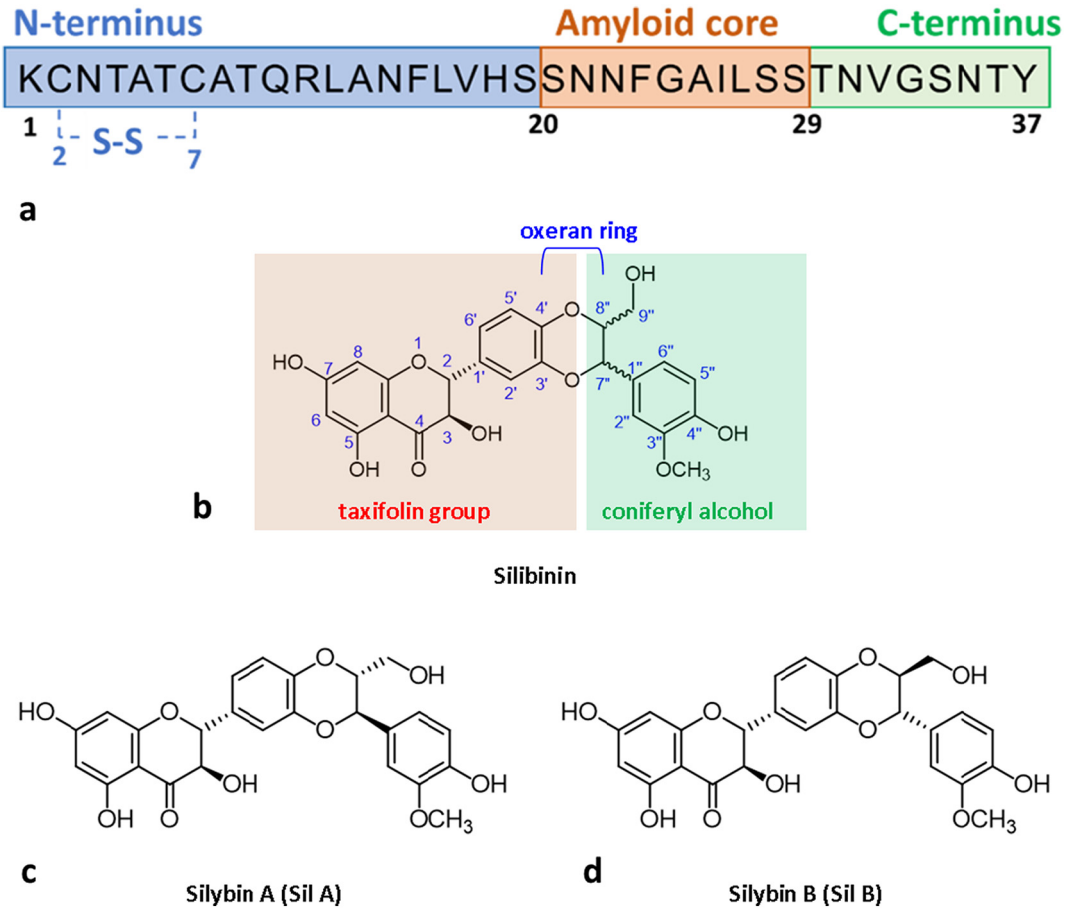

Fig. 1. (a) hIAPP sequence. The disulfide bridge is indicated as S—S. The N-terminus, the amyloid core, and the C-terminus are highlighted in different colors. (b) General chemical structure of silybins and nomenclature. Chemical structures of the two diastereoisomers (c) Silybin A and (d) Silybin B.

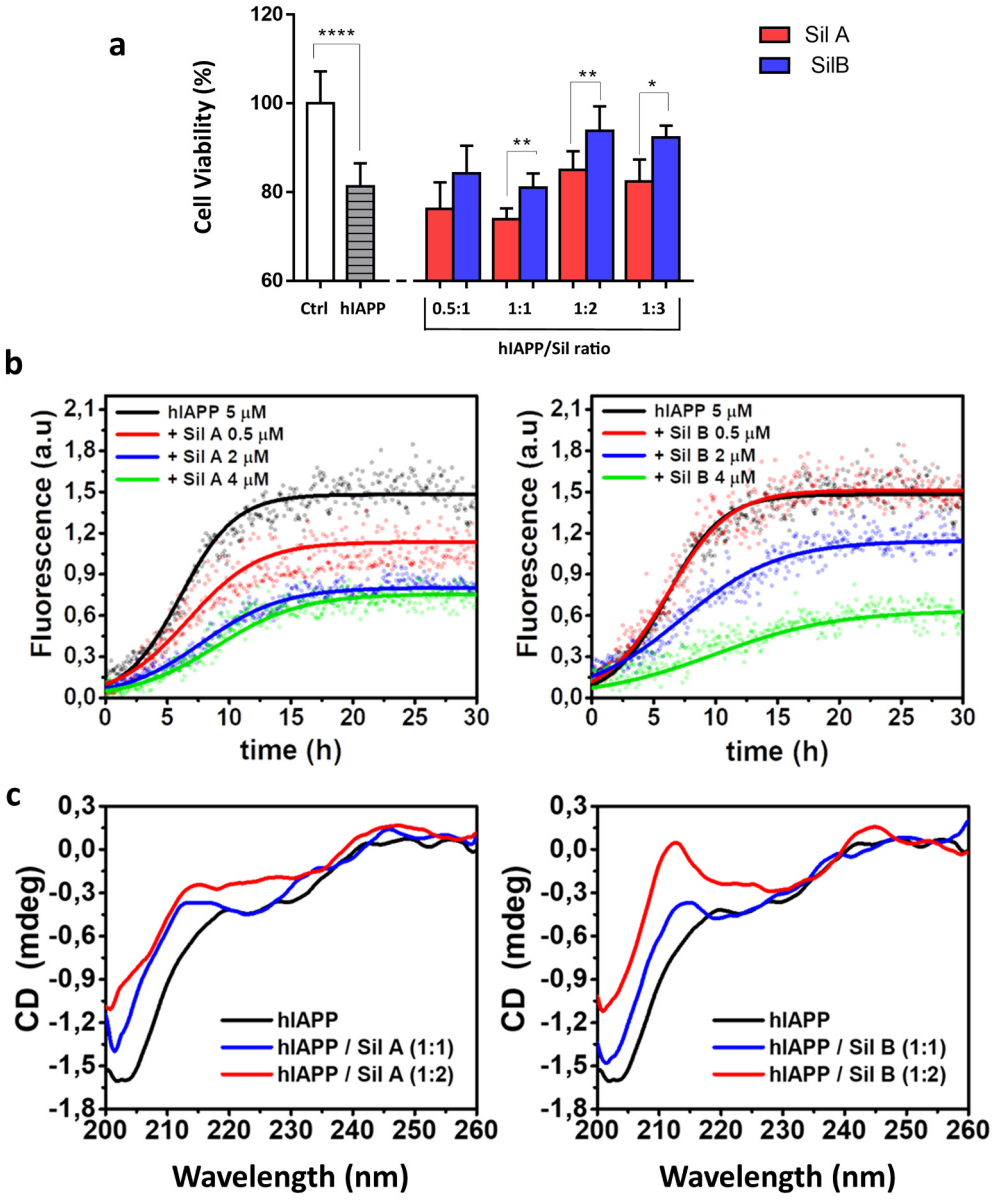

Fig. 2. (a) Dose-dependent Sil A (red bars) and Sil B (blue bars) attenuation of hIAPP-induced toxicity in rat insulinoma INS-1 cells. The effects of hIAPP is reported as a control (grey bar). Cell viability values of IAPP+Sil samples are normalized values calculated considering the effect of silybins at the same concentration (without hIAPP). Analysis of variance has been performed by One-way ANOVA followed by statistical Tukey's test (***$p < 0.01$; ***$p < 0.001$; ****$p < 0.0001$). The significant difference between the effect of both diastereoisomers has been determined by using the *t*-test (*$p < 0.05$; **p < 0.01). $N = 12$ biological replicates. (b) Amyloid fibrillation kinetics of hIAPP in absence (black curve) and presence of Sil A (left) or Sil B (right) in P/L molar ratios 1:0.1 (red curve), 1:0.4 (blue curve), and 1:0.8 (green curve). Dots represent experimental data; the continuous line is the fit of the kinetics obtained by averaging all characteristic parameters of the kinetics over three different experiments (see Table S1 in electronic supporting information). Experiments were carried out using hIAPP 5 μM at 25 °C in phosphate buffer 10 mM NaCl 100 mM pH 7.4. (c) Circular Dichroism spectra of human amylin in the absence (black line) and in the presence of Sil A (left) and Sil B (right) in P/L ratios 1:1 (blue line) and 1:2 (red line). CD curves have been registered at 4 °C in 10 mM phosphate buffer pH 7.4, incubation time max 10 min using a peptide concentration of 2.5 μM. (For interpretation of the references to colour in this figure legend, the reader is referred to the web version of this article.)

ratios. Due to the lower solubility of Silybins in pure water, ligand concentrations were optimized to allow a detectable amyloid growth and avoid ligand precipitation. In fact, because of the complex cellular milieu, Silybins could bind to other unknown components, implying that, in biological experiments, we need higher ligand concentrations to observe significant effects. Results show that both compounds reduce the maximum ThT intensity compared to control in a dose-dependent manner (Fig. 2b). Furthermore, both Sil A and Sil B slow down the aggregation kinetics which results in higher values of amyloid formation half time ($t_{1/2}$) than the control (Fig. 2b and table S1 in Electronic supporting information). At low ligand concentrations (P/L molar ratio 1:0.1) Sil A inhibits hIAPP aggregation better than Sil B (red lines in Fig. 2b). By contrast, at increasing ligand concentrations, Sil B exhibits a slightly better efficiency in reducing hIAPP aggregation than Sil A. In fact, Sil A reduces the percentage of formed fibrils of about 50% when added in a P/L molar ratio 1:0.8 (green lines in Fig. 2b), while the reduction in the presence of Sil B under the same conditions is of about 60%.

Circular Dichroism (CD) spectra of hIAPP/ligand mixtures further support the different effects of the two diastereoisomers on the conformations of hIAPP. Albeit addition of low doses (1:1 P/L molar ratio) of Sil A or Sil B to a freshly dissolved 2.5 μM hIAPP preparation did not affect the peptide random coil structure, a significant enhancement of a positive band at 212 nm was observed on Sil B addition at 1:2 P/L molar ratio (Fig. 1c). A positive CD band located at 212 nm is considered a signature of a polyproline II helix (PPII) structures [36], which have been reported to reduce the propensity of peptides to aggregate [37]. Hence, this shift in hIAPP conformation towards PPII structures reconciles with the different anti-aggregating effects observed in ThT experiments, showing a higher anti-fibrillogenic effect of Sil B.

2.2. Molecular dynamics of hIAPP/silybin complexes

Biological assays, ThT experiments and spectroscopic investigations provide strong evidence that Sil B when compared to Sil A, induces larger effects on the conformation of hIAPP, its aggregation and, eventually, toxicity. Low ligand solubility, the rugged conformational energetic profile of hIAPP and the weak and short-lived peptide/ligand interactions limit the mechanistic characterization of hIAPP/silybin complexes from a fully experimental perspective. Therefore, we

proceeded with performing molecular dynamics (MD) simulations to investigate the influence of the two silybin diastereoisomers on the structure of hIAPP.

Due to the high conformational flexibility of hIAPP, the selection of representative initial peptide structures deserves special consideration. First, we randomly generated seven independent conformations from the human peptide sequence (with the C2-C7 disulfide bridge). MD simulations were then performed independently for each structure for a total cumulated sampling of 6 μs. Five representative structures of the free peptide in solution were then identified using the SAPPHIRE (States And Pathways Projected with High Resolution) analysis [38] and used as initial configurations for the subsequent MD simulations with Sil A or Sil B (Fig. 3a and S2 of the electronic supporting information). For the production simulations, five starting systems were prepared all consisting of a peptide and Sil A or Sil B, respectively, each differing in the peptide/ligand (P/L) ratio, *i.e.,* 1:1 and 1:2. Ten independent simulations were carried out for each system for a cumulated sampling time of about 6.5 μs.

The results show different interaction preferences between the peptide and the diastereoisomers. The effect of the ligand concentration is evidenced in the interaction frequency between hIAPP and silybins. Sil A interacts for about 50% of the simulated time with hIAPP at 1:1 P/L ratio but the number of interactions decreases on increasing ligand concentrations. Sil B interacts with the peptide for 30% of the total simulation time and in a 1:2 P/L ratio Sil B forms twice as many contacts with the peptide (Fig. 3b). The contact frequency between Sil B and the peptide is dose dependent, while the interactions between Sil A and hIAPP appear to be independent of concentration. (Fig. 3c).

The contact map analysis (Fig. 4) reveals that in absence of ligands, the most frequent intramolecular contacts are observed in the first seven N-terminal residues (due to the presence of the disulfide bond) followed by the interactions between the amyloidogenic core (residues S20-S29) and the C7-L16 stretch in the N-terminus. In the presence of ligands, the matrices of intramolecular contacts are modified at several places. First, increased interactions between the stretches N14-S19 and T9-A13 of the N-terminus are recorded. Second, variable remodeling of the intra-peptide interactions between the amyloidogenic core and the N-terminus is observed, *i.e.,* interactions between stretches I26-V32 and F15-S20 are more abundant, contacts between the stretches N21-L27 and T6-Q10 are augmented, and the interactions between the stretches R11-L16 and N21-L27 are decreased. Third, the contacts between the C-terminal stretch T30-Y37 and the N-terminal residues K1-Q10 are reduced, while the interactions with the amyloidogenic core become more abundant.

An analysis of peptide flexibility reveals that silybins enhance the fluctuations of the amyloidogenic core and of more than half of the N-terminal residues (Fig. 5a and S3-S4). Additionally, the analysis of the contacts between the ligands and the peptide reveals that the most frequent contacts are recorded at the N-terminal stretch K1-L12, independently from ligand concentration (Fig. 5b and S5), followed by less abundant contact at the C-terminus and/or the amyloidogenic region. In a 1:1 P/L ratio, both Sil A and Sil B interact with the highest preference with residue R11 and the surrounding residues, *i.e.* A8-T9 and Q10, L12, respectively. At higher ligand concentration, the interaction frequencies of Sil A with hIAPP remain localized in the R11 region, yet significantly

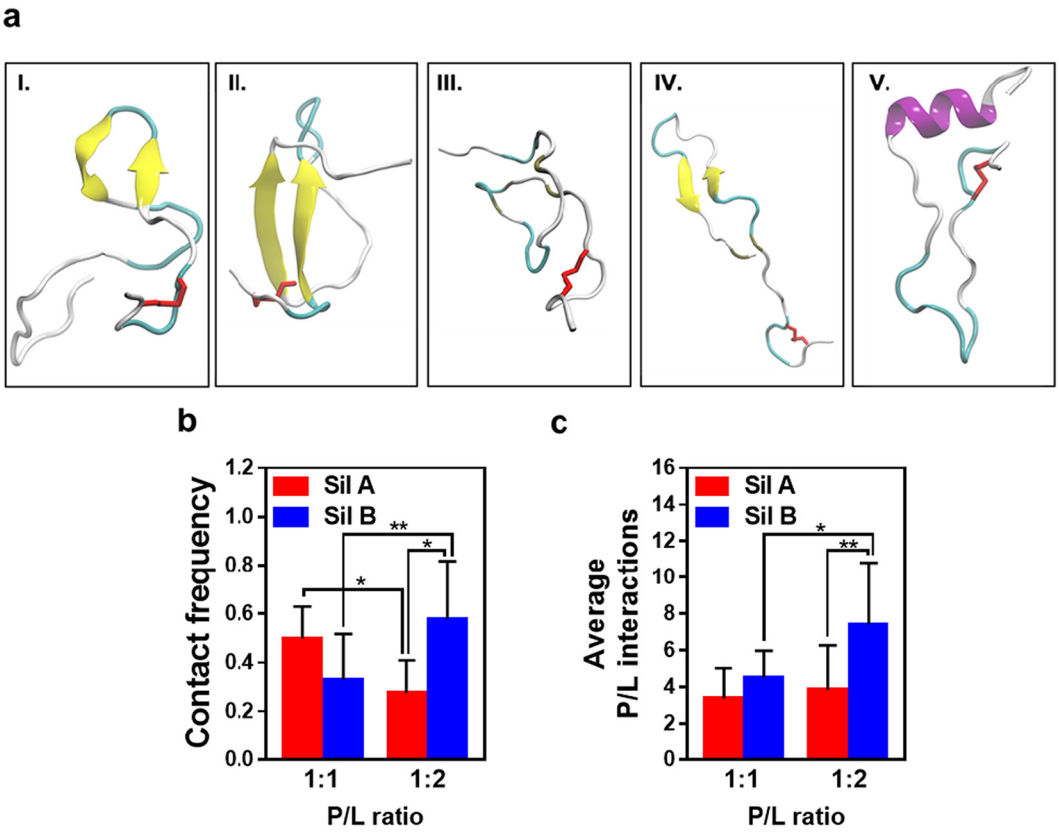

Fig. 3. (a) Starting hIAPP structures generated by the SAPPHIRE analysis. The red sticks represent the C2-C7 disulfide bridge. (b) Contact frequencies between hIAPP and Sil A (red bars) and Sil B (blue bars) in a peptide/ligand ratio 1:1 and 1:2. A contact is considered when the distance between any atoms of the ligand and the peptide is below 5 Å. The interacting time is normalized by the total number of snapshots and is represented as the average of 10 independent MD simulations for each system. Error bars represent the standard deviation of the 10 MD simulations. Analysis of variance has been performed by One-way ANOVA followed by statistical Tukey's test (*$p < 0.05$; **$p < 0.01$). (c) Average number of hIAPP-silybin contacts for systems containing Sil A (red bars) and Sil B (blue bars) simulated at a peptide/ligand ratio 1:1 and 1:2. Data are represented as the average of 10 independent MD simulations for each system. Error bars represent the standard deviation of the 10 MD simulations. Analysis of variance has been performed by One-way ANOVA followed by statistical Tukey's test (*p < 0.05; **p < 0.01). (For interpretation of the references to colour in this figure legend, the reader is referred to the web version of this article.)

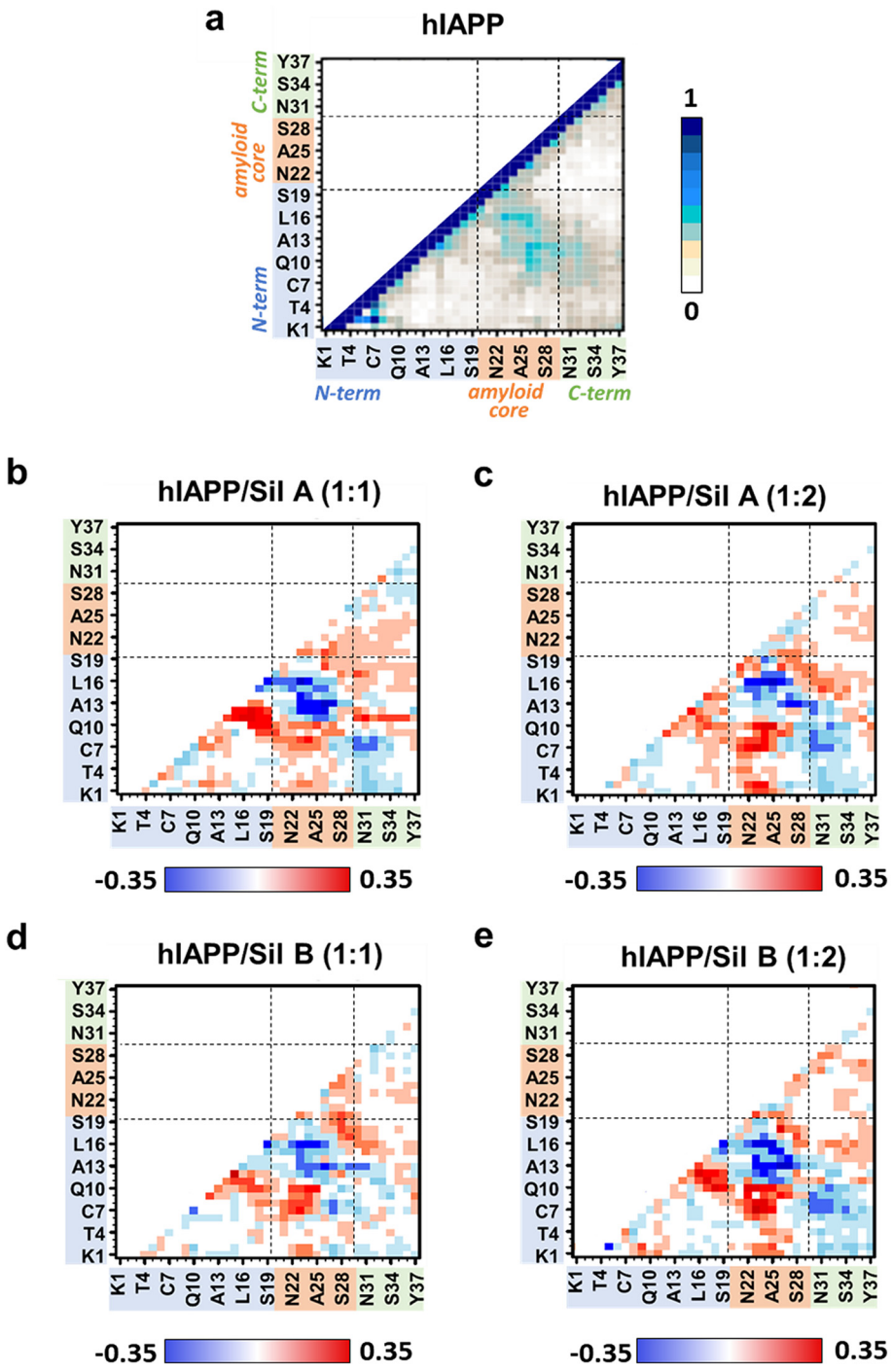

Fig. 4. Intramolecular contact frequencies. (a) The matrix of pairwise contacts for the monomeric hIAPP shows the absolute frequencies with dark blue representing the highest probability. (b-e) The other panels show differences relative to the system without ligands, highlighting more contacts in red and less contacts in blue. Two residues are considered to be in contact if the distance between any of their atoms is below 5 Å. (For interpretation of the references to colour in this figure legend, the reader is referred to the web version of this article.)

reduced when averaged per ligand. For Sil B, secondary interaction hotspots arise to encompass more residues in the N-terminus and in the amyloidogenic core. Sil B interacts preferentially with residue F23 from the amyloid core at 1:1 P/L ratio; but interacts with all the amyloid core residues (to a greater extent with residues S20, N21, N22, F23, I26 and L27) by increasing Sil B concentration. However, Sil A shows interactions with a more reduced number of residues (N21 F23 and L27) and, in this case, interactions decrease with the dose (Fig. 5b).

The interaction frequency between the closest groups of the ligand to hIAPP reveal that recurrent interactions between the deprotonated hydroxyl in position C-5 of both silybins and the cationic residues K1 and R11 are observed in all the explored conditions, thus suggesting that P/L interactions are partly driven by electrostatic forces. Due to the key role played by phenolic motifs in inhibiting the aggregation of amyloidogenic peptides [39–41], we evaluated the interactions of the peptide with the aromatic rings A, B, and E of each diastereoisomer. The results show more frequent interactions between Sil B and hIAPP, dominated by the involvement of rings B and E, as compared to the contacts formed by Sil A, which are guided by rings A and B (Fig. 5c). Interactions of hIAPP with ring E of Sil B are less evident in Sil A, due to the different chirality of the stereocenter located in C-7″. The methoxy and the hydroxyl groups in positions C-3″ and C-7 of both diastereoisomers interact significantly with hIAPP, but only the hydroxyl group in position 9″ of Sil B is in contact with the peptide. These interactions are more recurrent when Sil B is in 1:2 P/L molar ratio (Fig. 5c and Fig. S6).

The map of the P/L interactions shows that the aromatic rings of Sil A

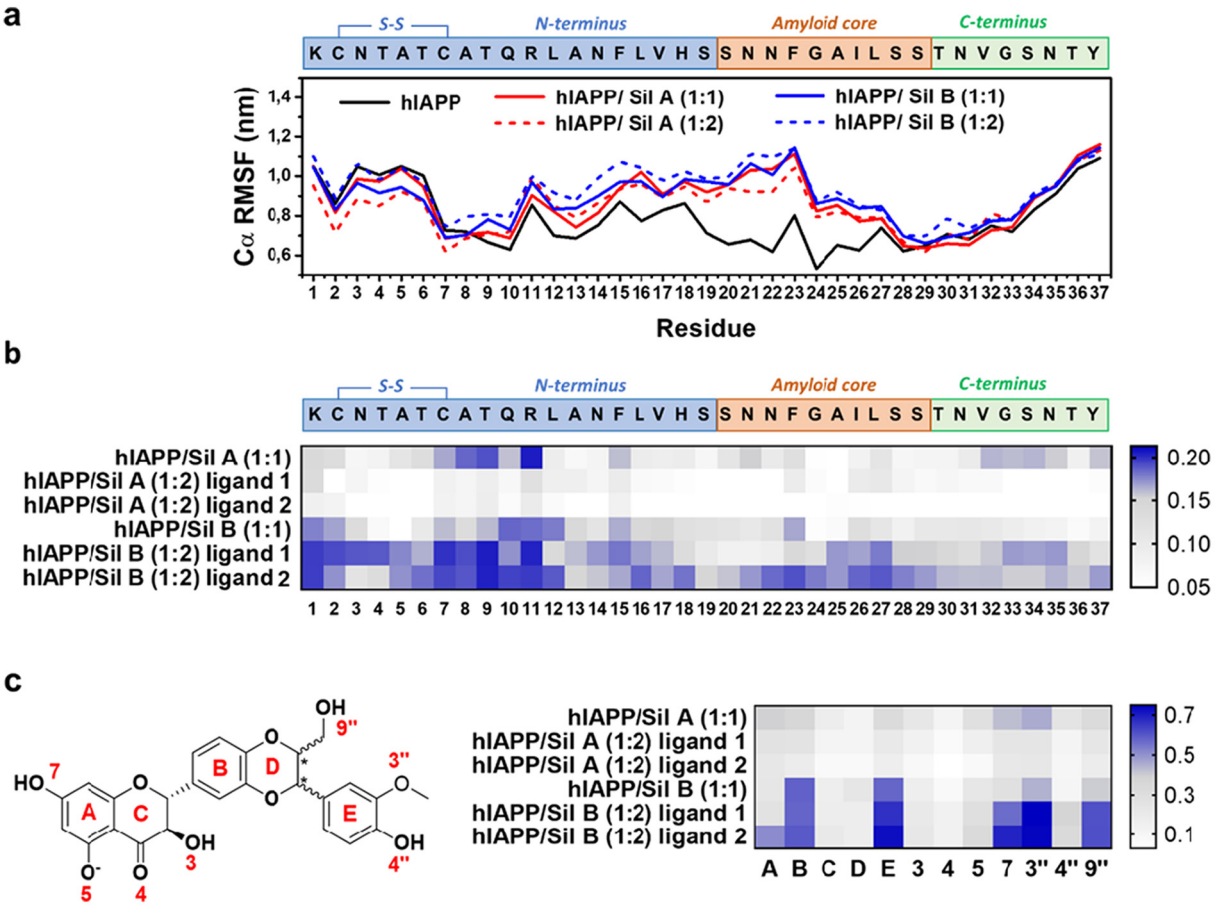

Fig. 5. (a) Root-mean-square fluctuations (RMSFs) of the C_α-atoms of hIAPP in the absence (black) and presence of Sil A (red) or Sil B (blue). The RMSF profiles were calculated as the average over 20 independent 300-ns profiles. The fluctuations were calculated about the average structures determined from the 300 ns run excerpts. (b) Interaction sites between the ligands and hIAPP mapped on the sequence of the peptide and (c) on the sequence of the ligands. Two units are considered to be in contact if the distance between any of their atoms is shorter than 5 Å. The interaction mapped on the sequence of the ligands takes into account only single contacts formed with the specific groups, *i.e.* only the closest group is considered to be in contact with hIAPP. The nomenclature used for the ligand groups is reported on the left. (For interpretation of the references to colour in this figure legend, the reader is referred to the web version of this article.)

were involved in interactions with several residues (*i.e.* K1-F2, A5-R11, F15, S20-N21, F23, L27, N31-N35, and Y37). However, in presence of two Sil A molecules, interactions with these aromatic rings resulted much less frequent (Fig. 6). Sil B interacted with hIAPP through their aromatic rings involving the peptide residues K1-N3, A5-V17, S20-F23, L27, and N31-G33. But, unlike Sil A, interactions with hIAPP through Sil B aromatic rings became more recurrent in simulations at 1:2 P/L ratio of Sil B, including new interactions (*i.e.* T4, H18, G24-I26, S28-S29, S34-Y37) in addition to the above-mentioned ones.

The distributions of the backbone dihedral angles φ and Ψ (Ramachandran plots) allow to evaluate the conformational changes induced by the ligands onto hIAPP. The results show that the molecules have a comparable effect on the conformation of hIAPP in the simulations with P/L ratio 1:1 (Fig. 7a and c), characterized by a decrease in α_R content ($\varphi \sim 80°$; $\Psi \sim 0°$), slight increase in α_L conformations ($\varphi \sim -60°$; $\Psi \sim -60°$) and more abundant PPII structures ($\varphi \sim -60°$; $\Psi \sim 150°$). Additionally, the decrease in α_R content is more evident in the simulations performed at an equimolar ratio as compared to the simulations performed in the presence of two ligand molecules. At higher ligand concentrations, Sil A has marginal effects on the conformations sampled by hIAPP (as compared to P/L ratio 1:1), while Sil B additionally induces a decrease of β-rich structures (Fig. 7d). The decrease in β-sheet content in presence of Sil B correlates with the higher antiaggregant ability of this diastereoisomer. These data are consistent with ThT assays where, at lower concentrations, Sil A presented a higher impact as anti-aggregant compound than Sil B, while Sil B was more effective than its diastereoisomer at higher concentration. Notably, independently of the ligand concentration, the peptide samples more PPII structures, which are commonly formed at the expenses of a reduction in the β sheet content [36]. Importantly, the increase in PPII content is consistent with the CD measurements.

3. Discussion

Despite extensive efforts, the development of synthetic anti-diabetic compounds able to attenuate IAPP aggregation and toxicity has been so far hampered by the occurrence of severe side effects and poor clinical profiles [42]. Small molecules extracted from natural sources, due to their distinctive structural variety, are emerging as valuable suppliers of bioactive chemical scaffolds, with favorable safety profiles and attractive pharmacological properties [43]. These compounds have been suggested to inhibit human IAPP aggregation by establishing weak interactions with monomeric IAPP preventing inter-peptide interactions and, eventually amyloid-like aggregation into toxic aggregates [44,45]. However, a detailed characterization of their effects at molecular level remains elusive. Many natural drugs, including silybins, are commonly used as a mixture of stereoisomers (diastereisomers/enantiomers). Although stereoisomers are normally difficult to be discriminated in the lab, they are readily distinguished in the body and may significantly differ in their biological effects and, ultimately, therapeutic properties. Eventually, whether to use a mixture or a single stereoisomer in therapeutic applications is a complex decision to which a detailed

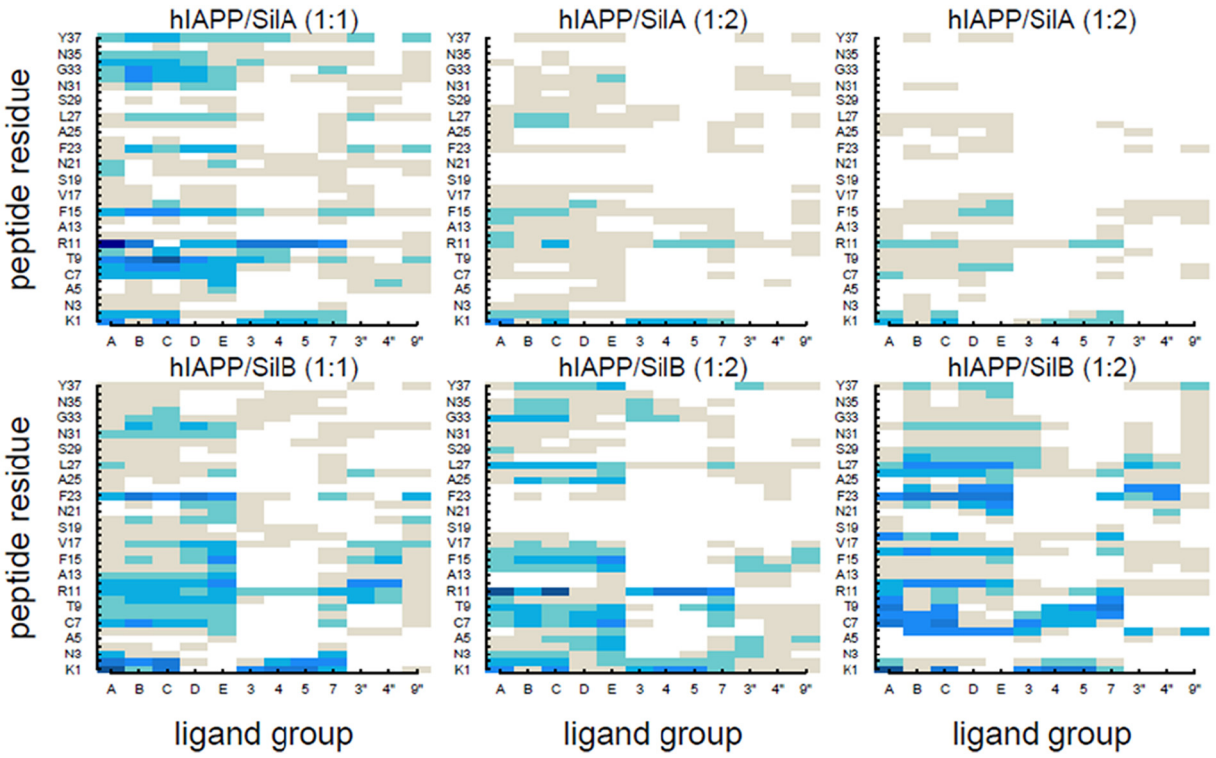

Fig. 6. Contact maps (threshold distance of 5 Å) of hIAPP with Sil A or Sil B at 1:1 and 1:2 P/L molar ratios.

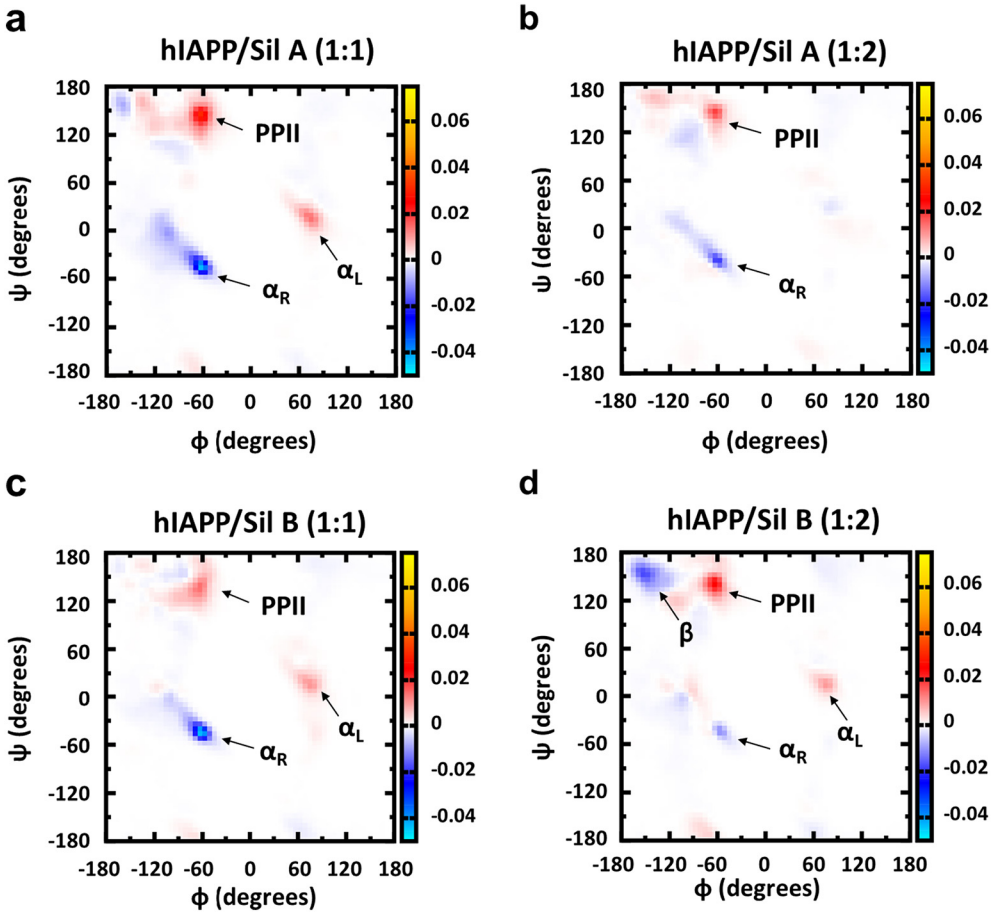

Fig. 7. Ramachandran plots. (a) Changes in the probability distribution of backbone dihedral angles of hIAPP induced by the presence of SilA in a P/L ratio 1:1. The plot has been obtained by subtracting the Ramachandran probability distribution of hIAPP alone from that one in the presence of Sil A in the specified conditions. Red and blue regions in the plot correspond to positive and negative values, respectively, and thus, with an increase or decrease in the probability of these dihedral angles. (b) As (a) except for 1:2 ratio. (c) As (a) except for Sil B. (d) As (b) except for Sil B. (For interpretation of the references to colour in this figure legend, the reader is referred to the web version of this article.)

comprehension of the action mechanism must make a significant contribution.

Some of us have recently probed the critical role played by the stereochemistry of these compounds in inhibiting Aβ aggregation in aqueous media, being Sil B more active than Sil A due to different interactions with Aβ [46,47]. Furthermore, it has been reported that Sil B is more effective than Sil A in inhibiting lysozyme fibrillation [48]. In analogy with Aβ and lysozyme, here we evidence that Sil B may interact with hIAPP regions that are key players in peptide aggregation. Indeed, albeit both diastereoisomers have been found to inducing changes in the conformational space of hIAPP, some significant differences in their binding to hIAPP do exist and should be considered for a comprehensive understanding of their inhibition mechanism.

Early reports demonstrated that an isolated peptide encompassing the sequence S20-S29 of IAPP may form amyloid fibrils in aqueous solution [8]. Our MD simulations show that the presence of silybins increases the flexibility of the S20-S29 domain. Moreover, we find that Sil B, more than Sil A, interacts with the amyloidogenic core of the peptide, and contributes to the reduction the β-sheet content of the peptide at high concentration. Consequently, the conformational change and the increased PPII content can explains the lower propensity of hIAPP to aggregate into amyloid fibrils in the presence of the ligand. The N-terminal region of IAPP has been also shown to influence IAPP aggregation and the highly conserved disulfide bonds linking C2 with C7 is essential to inhibit IAPP aggregation [49,50] by stabilizing α-helical conformation [51]. Moreover, the N-terminal part of IAPP inserts into lipid membranes [52–54] and is believed to play a major role in modulating peptide toxicity [55–57]. Notably, Sil B interacts with all residues in the region encompassing residues K1-L12 and this may explain the mitigating effect of Sil B in counteracting hIAPP toxicity to INS-1 cells. ThT assays are in line with data concerning the ligand/peptide interaction frequencies: Sil A presents higher interaction frequency than Sil B when is at 1:1 P/L ratio, but at higher (1:2) Sil B is more effective (see Fig. 2b).

Experimental evidence indicates that aromatic side chains seed IAPP amyloid growth. In particular, the role played by the phenylalanines F15 and F23 has been widely investigated although their specific contributions in driving IAPP self-assembly are still debated [58–62]. MD simulations of hIAPP/silybin shown important interactions of the ligands, through their aromatic rings, with the side chains of F15 and F23. These interactions are more recurrent for Sil B than Sil A. Residues S20-S29 are supposed to be key determinants driving full-length IAPP amyloid growth [63]. MD simulations of hIAPP/silybin demonstrated that the aromatic rings of silybins interact with some residues forming part of this region. Sil A shows interactions with residues S20, N21 F23 and L27 while Sil B interacts with all the amyloid core residues, to a greater extent with residues S20, N21, N22, F23, I26 and L27. At a 1:2 P/L ratio the interactions between Sil B and the amyloid core increase, differently as compared to Sil A. Consequent to these interactions with the Sil B, some residues of the amyloid core underwent a β-sheet - > α-helix and PPII conformational transition which provides a structural explanation of the lower propensity of hIAPP to aggregate into amyloid fibrils in the presence of the ligand.

The steric hindrance caused by the OH moiety connected to the D group in Sil B is expected to inhibit the E aromatic ring from rotating freely. By contrast, the aromatic group of Sil A is flexible, making the molecule more prone to interact with hIAPP aromatic groups and other hydrophobic residues. In Sil B, however, this contact is not possible, and polar interactions *via* the hydrophobic C-terminus predominate. Therefore SilB/hIAPP interactions are mostly ascribed to polar 9″-OH and 3″-OCH3 groups, which may be a primary driving force.

H18 is also believed to be a key player in driving IAPP aggregation. In particular, the protonation state of H18 participate to IAPP aggregation by regulating intermolecular electrostatic forces [64]. MD simulations showed that, while Sil A does not present contacts with this residue, the hydroxyl group 7 of Sil B interact with residue H18 (Fig. 6). The aromatic rings A and C of Sil B are also in contact with H18, and this may contribute to hinder both polar and non-polar intermolecular contacts mediated by this residue.

Asparagine residues have been proposed to play an important role in IAPP aggregation and in particular in the formation of small sized oligomers [56,65,66]. Deamidation of asparagine, which may occur without enzymatic assistance, may seed IAPP aggregation [65,67–69]. Sil A interact with N35 through its aromatic rings at 1:1 P/L ratio while, at higher dose, these interactions are not present. Differently, interactions with residue N35 are not present when Sil B is studied at 1:1 P/L ratio, but at 1:2 P/L ratio Sil B establish polar and non-polar interactions through ring B and C and hydroxyl group in position 3.

The N-terminal region of IAPP has been also shown to influence IAPP aggregation and the highly conserved disulfide bonds linking C2 with C7 is essential to inhibit IAPP aggregation [49,50] by stabilizing α-helical conformation [51]. Moreover, the N-terminal part of IAPP inserts into lipid membranes [52–54] and is believed to play a major role in modulating peptide toxicity [55–57]. Notably, Sil B shows more interactions than Sil A with this region, and are more abundant at 1:2 P/L ratio. Sil B interacts with all residues in the region encompassing residues K1-L12 and this may explain the mitigating effect of Sil B in counteracting hIAPP toxicity to INS-1 cells.

In conclusion, we have provided evidence that Sil B is an effective inhibitor of hIAPP toxic self-assembly *in vitro*, and have characterized the molecular mechanisms and atomistic details of the Sil B and Sil A interactions with hIAPP by biophysical methods and atomistic simulations. Sil B has potential as drug candidate for T2D chemoprevention and therapy. Our work underlines the value of multidisciplinary studies of amyloid self-assembly inhibition, and shows the importance of a comprehensive knowledge of the stereochemistry of natural compounds for the development of potent antifibrillogenic agents.

4. Materials and methods

4.1. Chemicals

Human Islet Amyloid Polypeptide (hIAPP) was purchased from GenScript. High purity MeCN and MeOH were purchased from Carlo Erba Reagents. All chemical reactants, including silibinin, were purchased from Sigma-Aldrich. Sil A and Sil B were extracted from commercial silibinin by HPLC according to a protocol reported elsewhere [70].

4.2. hIAPP samples preparation

hIAPP was solubilized in hexafluoroisopropanol (HFIP) at 1 mg/mL, incubated over night at room temperature to dissolve preformed aggregates, aliquoted (100 μL/aliquot), frozen at −80 °C and lyophilized. Peptide aliquots were quantified by solving hIAPP powder in 20 μL of DMSO or NaOH 1 mM, respectively, adding it to 180 μL of buffer (phosphate 10 mM, pH 7.4) and by routinely checking the optical absorbance at 280 nm ($\varepsilon_{HIAPP} = 1615\ M^{-1}\ cm^{-1}$). hIAPP aliquots were resuspended in the cell medium just prior the toxicity experiments.

4.3. hIAPP aggregation - ThT assays

Samples were prepared by adding 1 μL of the studied molecule DMSO stock solutions to 50 μL of ThT 20 μM in PBS (phosphate 10 mM, pH 7.4, 100 mM NaCl). Experiments were carried out in 384-well plates. Immediately after the addition of hIAPP (previously monomerized by the above-described protocol; 5 μM) time traces were recorded using a Varioskan plate reader (ThermoFisher, Waltham, MA) with λ_{exc} 440 nm and λ_{em} 480 nm at 37 °C. The plate was shaken for 10 s before each read (600 shakes per minute with a diameter of the orbital movement of 1 mm) to avoid the fibrils precipitation. Final DMSO concentration was maintained at 2% and controls in its presence and absence were carried out to exclude possible changes in hIAPP aggregation kinetics due to its

presence. Controls in the absence of hIAPP were also performed for each tested condition to exclude false ThT positive signals unrelated to amyloid. Each condition was tested in triplicate and data were expressed as the average of the kinetic parameters obtained by fitting each of the replicas and are reported in table S1 as mean (standard deviation). The characteristic parameters of hIAPP aggregation were obtained by fitting each kinetic curve with the following equation:

$$I = \frac{I_{max}}{1 + e^{k \cdot (t - t_{1/2})}}$$

where I is the fluorescence intensity as a function of time t, I_{max} corresponds to the maximum intensity of fluorescence, k is the apparent rate constant, $t_{1/2}$ and lag time (t_{lag}) represent the point in time where the signal reaches 50% and 10% of the amplitude of the transition, respectively.

4.4. Cell culture

Pancreatic insulinoma INS-1 cells from *Rattus norvegicus*, kindly donated by Prof. S. Piro from University of Catania, were cultured in Roswell Park Memorial Institute (RPMI) 1640 medium (Gibco), supplemented with 10% (v/v) fetal bovine serum (Gibco), penicillin 100 U/mL, streptomycin 100 μg/mL, 1 mM sodium pyruvate (Sigma), 2 mM L-glutamine (Gibco), 10 mM HEPES (4-(2-hydroxyethyl)-1-piperazineethanesulfonic acid) (Sigma Aldrich) and 0.05 mM β-mercapto-EtOH (Thermo) maintained at 37 °C, 5% CO_2, and 95% relative humidity in tissue culture flasks (Eppendorf). Cultures were routinely split (1:3) at ~80% confluency by rinsing the cells with Hank's buffer without calcium or magnesium and released for sub-cultivation using 0.25% (v/v) trypsin-EDTA.

4.5. Cell viability tests

Cells at ~80% confluency (passage number 28–34) were detached from culture using 0.25% trypsin-EDTA, rinsed, then plated at a density of 50,000 cells per well in 200 μL of medium in a 96-well plate (Eppendorf) for 48 h. Then a starved serum condition (FCS 3%) was performed; this started 24 h before the hIAPP-silybins treatment. hIAPP was suspended in the RPMI1640 at a concentration of 5 μM, without fetal bovine serum (FBS) and without other medium components (L-glutamine, sodium pyruvate Hepes, β-mercapto-EtOH) and pre-incubated for 10 h at 27 °C, in the absence of cells. The duration of the hIAPP/ligand incubation step was set for 10 h at 25 °C to allow the formation of toxic oligomers and protofibrils, relying on a previous ThT experiment performed in the cell culture medium at 25 °C (data not shown) that indicated an amyloid formation half time ($t_{1/2}$) of 10.8 ± 2.5 h (95% CI) under these experimental conditions. Cell viability (Fig. 2a) was reported as normalized values with respect to controls (with silybins at the same concentration and without hIAPP),

Then a solution of FCS at 1%, L-glutamine, sodium pyruvate Hepes, β-mercapto-EtOH was added to medium/hIAPP solutions and then these last were transferred in the cells. Based on preliminary hIAPP aggregation assays carried out in culture medium RPMI 1640, we determined the optimal incubation time at which silybins showed the best anti-aggregating hIAPP abilities. Thus, these experimental conditions (hIAPP-silybins incubation for 10 h) were used for cell viability MTT experiments. After 21 h the cell viability was assessed using the 3-(4,5-dimethyl-2-thiazolyl)-2,5-diphenyl-2H tetrazolium bromide (MTT; Sigma) tetrazolium salt reduction assay. Cells were incubated in a 0.5 mg/mL MTT solution (in RPMI1640) for 4 h at 37 °C; the intensity of (the formazan produced from enzyme cleavage of the tetrazolium salt by metabolically active cells is proportional to the number of viable cells). The medium was removed and DMSO was added to solubilize the MTT formazan crystals. The plate was mixed for 30 min and the absorbance (570 nm) was measured using a plate-reader (Varioskan Thermo). Data are expressed as the percentage of MTT reduction respect the untreated cells (positive control). Mean values were compared to data for untreated control cells using ANOVA test.

4.6. Circular Dichroism (CD)

CD measurements were performed by a Jasco J-810 spectropolarimeter using quartz cuvettes with 1 cm of optical path at 4 °C from 260 nm to 200 nm. 2.5 μM hIAPP solutions were prepared in 100 mM phosphate buffer pH 7.4, from freshly prepared peptide aliquots monomerized according to the above-mentioned protocol and immediately analyzed to prevent aggregation. CD spectra were recovered after adding increasing concentrations of Sil A, Sil B, from aqueous 1 mM stock solution. The pH of silybin stock solutions was previously fixed to 10.2 to prevent ligand aggregation. Reported spectra were obtained by routinely subtracting the ligand spectrum at the same concentration.

4.7. Molecular dynamics

4.7.1. Ligand preparation

The structures of Silybin A and Silybin B were extracted from our previous study [70] and the CHARMM General Force Field (CgenFF) [71,72] was used to generate the partial charges. Following experimental results reported elsewhere [33], we use silybins mono-deprotonated at position C-5 for the present study.

4.7.2. Initial hIAPP structures

We first generated seven independent random starting configurations for hIAPP using Monte Carlo sampling. More precisely, the 37 residues were initially built in an excluded volume-obeying manner using CAMPARIv3 (http://campari.sourceforge.net) while preserving the C2-C7 disulfide bond. This procedure randomizes dihedral angles hierarchically and guarantees that there is no spurious correlation between the starting models. Each structure was then minimized using CAMPARIv3 for 100,000 elementary Monte Carlo steps. Seven independent molecular dynamics simulations (following the same protocol as described in the Molecular dynamics Section) were carried out in the NVT ensemble cumulating 6 μs. Snapshots were saved every 50 ps. From the total cumulated sampling five representative snapshots of hIAPP were extracted and posteriorly used as starting structures in the simulations with hIAPP/silybins complexes. To identify the representative snapshots, we used the SAPPHIRE (States And Pathways Projected with High Resolution) analysis. SAPPHIRE is a computational method developed to capture in a single illustration the states sampled by a complex system and the order in which they are visited along one or multiple trajectories, assigning their statistical weight and the recurrence with which are visited along one or multiple trajectories [38]. The essential idea is to generate a one-dimensional plot which allows the partition of the entire sampling into free energy basins based on the similarity between the simulation snapshots as defined by a specific geometric parameter given as input. Briefly, starting from a random snapshot (*i.e.* simulation frame) the remaining snapshots are ordered such that the frame closest to any prior entry in the sequence becomes the next item in the array data. This allows the sorting of the data into sets of basins consisting of similar snapshots. The resulting sequence of snapshots is referred to as progress index. We defined the metric as the RMSD of the ψ-angles of the residues at the core of the peptide, *i.e.* T9-S28 excluding residues H18- G24. The latter stretch, residues K1-A8 and S29-V37 were excluded due to their lack of significant structuring throughout the simulations leading to no discriminatory signals. The barriers on the cut function (local minima and maxima on the profile in black in Fig. S2) enable the identification of individual metastable states. Thus, the local minima of the cut function correspond with the highly populated states while the local maxima are barriers, *i.e.* conformational states visited sporadically. The progress index is usually annotated with several geometric variables, which are helpful to visually characterize

the states. In this sense, the secondary structure assignment per residue was added on top (Fig. S2). From the basins, which show frequent recurrence (*i.e. many red dots separated by grey dashed lines in the kinetic trace*), we selected five representative snapshots to be used as input structures for the subsequent hIAPP-silybin simulations.

4.7.3. Molecular dynamics simulations

All simulations were carried out using the GROMACS 2018.6 simulation package [73] and the CHARMM36m force field [74]. Four simulation systems were prepared consisting of a peptide and Sil A or Sil B, respectively, each system differing in the peptide/ligand (P/L) ratio, *i.e.,* 1:1 and 1:2. Ten independent simulations were carried out for each system for a total sampling time of 6–7 μs. Snapshots were saved every 50 ps. To reproduce neutral pH conditions, the Arg and Lys side chains and the N-terminus were positively charged, while the Asp and Glu side chains and the C-terminus were negatively charged. Each system was solvated in a cubic box (12.8 nm edge length) with TIP3P water molecules [75] to which 150 mM NaCl was added, including neutralizing counterions. Periodic boundary conditions were applied. Following steepest descent minimization, the systems were equilibrated under constant pressure for 1 ns, with position restraints applied on the heavy atoms of the complexes. For the production runs, temperature and pressure were maintained constant at 310 K and 1 atm, respectively, by using the modified Berendsen thermostat [76] (0.1 ps coupling) and barostat [77] (2 ps coupling). The short-range interactions were cut off beyond a distance of 1.2 nm, and the potential smoothly decays to zero using a Verlet cutoff scheme. For the electrostatics, the Particle Mesh Ewald (PME) method with a cubic interpolation order and a grid spacing for Fast Fourier Transform (FFT) of 0.16 nm were used. To constrain all-bonds length the LINCS algorithm (fourth-order, 2 iterations) was used. The time step of simulations was fixed to 2 fs and periodic boundary conditions were applied. All simulations were performed on the Piz Daint supercomputer at the Swiss National Supercomputing Centre (CSCS).

CRediT authorship contribution statement

Sara García-Viñuales: Investigation, Formal analysis. **Ioana M. Ilie:** Supervision and investigation, Formal analysis, Writing - review and editing. **Anna Maria Santoro:** Investigation, Formal analysis. **Valeria Romanucci:** Resources. **Armando Zarrelli:** Resources. **Giovanni Di Fabio:** Resources. **Amedeo Caflisch:** Supervision, Writing – review & editing. **Danilo Milardi:** Writing – original draft, Supervision.

Declaration of Competing Interest

The authors declare no conflicts of interest.

Acknowledgements

S.G.V. is grateful to the European Union Horizon 2020 research and innovation program for funding her PhD fellowships under the Marie Sklodowska-Curie grant agreement INCIPIT n. 665403. I.M.I. thanks the Peter und Traudl Engelhorn Foundation for a postdoctoral fellowship. The computational resources were provided by the Swiss National Supercomputing Centre (CSCS) in Lugano. We also acknowledge AIP-RAS Onlus (Associazione Italiana per la Promozione delle Ricerche sull'Ambiente e la Salute umana) for grants in support of this investigation.

Appendix A. Supplementary data

Supplementary data to this article can be found online at https://doi.org/10.1016/j.bbapap.2022.140772.

References

[1] American Diabetes Association, Diagnosis and classification of diabetes mellitus, Diabetes Care 32 (2009) S62–S67, https://doi.org/10.2337/dc09-S062.
[2] D.P. Singal, M.A. Blajchman, Histocompatibility (HL-A) antigens, lymphocytotoxic antibodies and tissue antibodies in patients with diabetes mellitus, Diabetes 22 (1973) 429–432.
[3] J. Nerup, P. Platz, O.O. Andersen, M. Christy, J. Lyngsoe, J.E. Poulsen, L.P. Ryder, L.S. Nielsen, M. Thomsen, A. Svejgaard, HL-A antigens and diabetes mellitus, Lancet 2 (1974) 864–866.
[4] IDF Diabetes Atlas. www.diabetesatlas.org, 2019.
[5] R. Goyal, I. Jialal, Diabetes mellitus type 2, in: StatPearls, StatPearls Publishing, Treasure Island (FL), 2020. http://www.ncbi.nlm.nih.gov/books/NBK513253/ (accessed May 22, 2020).
[6] D. Milardi, E. Gazit, S.E. Radford, Y. Xu, R.U. Gallardo, A. Caflisch, G. T. Westermark, P. Westermark, C.L. Rosa, A. Ramamoorthy, Proteostasis of islet amyloid polypeptide: a molecular perspective of risk factors and protective strategies for type II diabetes, Chem. Rev. 121 (2021) 1845–1893, https://doi.org/10.1021/acs.chemrev.0c00981.
[7] P. Westermark, A. Andersson, G.T. Westermark, Islet amyloid polypeptide, islet amyloid and diabetes mellitus, Physiol. Rev. 91 (2011).
[8] P. Westermark, U. Engström, K.H. Johnson, G.T. Westermark, C. Betsholtz, Islet amyloid polypeptide: pinpointing amino acid residues linked to amyloid fibril formation, PNAS 87 (1990) 5036–5040.
[9] M. Anguiano, R.J. Nowak, P.T. Lansbury, Protofibrillar islet amyloid polypeptide permeabilizes synthetic vesicles by a pore-like mechanism that may be relevant to type II diabetes, Biochemistry 41 (2002) 11338–11343.
[10] K. Sasahara, Membrane-mediated amyloid deposition of human islet amyloid polypeptide, Biophys. Rev. 10 (2018) 453–462.
[11] G. Liang, J. Zhao, X. Yu, J. Zheng, Comparative molecular dynamics study of human islet amyloid polypeptide (IAPP) and rat IAPP oligomers, Biochemistry 52 (2013) 1089–1100, https://doi.org/10.1021/bi301525e.
[12] I.M. Ilie, A. Caflisch, Simulation studies of amyloidogenic polypeptides and their aggregates, Chem. Rev. (2019), https://doi.org/10.1021/acs.chemrev.8b00731.
[13] L. Khemtémourian, M.F.M. Engel, R.M.J. Liskamp, J.W.M. Höppener, J.A. Killian, The N-terminal fragment of human islet amyloid polypeptide is non-fibrillogenic in the presence of membranes and does not cause leakage of bilayers of physiologically relevant lipid composition, Biochim. Biophys. Acta 1798 (2010) 1805–1811, https://doi.org/10.1016/j.bbamem.2010.05.022.
[14] R.P.R. Nanga, J.R. Brender, J. Xu, G. Veglia, A. Ramamoorthy, Structures of rat and human islet amyloid polypeptide IAPP(1-19) in micelles by NMR spectroscopy, Biochemistry 47 (2008) 12689–12697, https://doi.org/10.1021/bi8014357.
[15] S. Gilead, E. Gazit, The role of the 14–20 domain of the islet amyloid polypeptide in amyloid formation, Exp. Diabetes Res. 2008 (2008), 256954, https://doi.org/10.1155/2008/256954.
[16] P. Cao, F. Meng, A. Abedini, D.P. Raleigh, The ability of rodent islet amyloid polypeptide to inhibit amyloid formation by human islet amyloid polypeptide has important implications for the mechanism of amyloid formation and the design of inhibitors, Biochemistry 49 (2010) 872–881, https://doi.org/10.1021/bi901751b.
[17] P. Westermark, U. Engström, K.H. Johnson, G.T. Westermark, C. Betsholtz, Islet amyloid polypeptide: pinpointing amino acid residues linked to amyloid fibril formation, Proc. Natl. Acad. Sci. U. S. A. 87 (1990) 5036–5040.
[18] M.R. Nilsson, D.P. Raleigh, Analysis of amylin cleavage products provides new insights into the amyloidogenic region of human amylin1 1Edited by P. E. Wright, J. Mol. Biol. 294 (1999) 1375–1385, https://doi.org/10.1006/jmbi.1999.3286.
[19] B. Ren, Tanshinones inhibit hIAPP aggregation, disaggregate preformed hIAPP fibrils, and protect cultured cells, J. Mater. Chem. B 6 (2018) 56–67.
[20] S. Asthana, M. Sahu, P.S. Nayak, B. Mallick, S. Jha, The smaller heparin fragments bind non-specifically through the IAPP sequence: an in silico study, Int. J. Biol. Macromol. 113 (2018) 1092–1104, https://doi.org/10.1016/j.ijbiomac.2018.03.001.
[21] I. Fernández-Gómez, M. Sablón-Carrazana, A. Bencomo-Martínez, G. Domínguez, R. Lara-Martínez, N.F. Altamirano-Bustamante, L.F. Jiménez-García, K. Pasten-Hidalgo, R.A. Castillo-Rodríguez, P. Altamirano, S.R. Marrero, C. Revilla-Monsalve, P. Valdés-Sosa, F. Salamanca-Gómez, E. Garrido-Magaña, C. Rodríguez-Tanty, M. M. Altamirano-Bustamante, Diabetes drug discovery: hIAPP1–37 polymorphic amyloid structures as novel therapeutic targets, Molecules 23 (2018) 686, https://doi.org/10.3390/molecules23030686.
[22] S.K. Azzam, H. Jang, M.C. Choi, H. Alsafar, S. Lukman, S. Lee, Inhibition of human amylin aggregation and cellular toxicity by lipoic acid and ascorbic acid, Mol. Pharm. 15 (2018) 2098–2106, https://doi.org/10.1021/acs.molpharmaceut.7b01009.
[23] A. Kakinen, J. Adamcik, B. Wang, X. Ge, R. Mezzenga, T.P. Davis, F. Ding, P.C. Ke, Nanoscale inhibition of polymorphic and ambidextrous IAPP amyloid aggregation with small molecules, Nano Res. 11 (2018) 3636–3647, https://doi.org/10.1007/s12274-017-1930-7.
[24] F. Lolicato, A. Raudino, D. Milardi, C. La Rosa, Resveratrol interferes with the aggregation of membrane-bound human-IAPP: a molecular dynamics study, Eur. J. Med. Chem. 92 (2015) 876–881.
[25] S.U.B. Farrukh, I. Javed, A.Q. Ather, A.-H. Emwas, M. Alazmi, X. Gao, G. A. Chotana, T.P. Davis, P.C. Ke, R.S.Z. Saleem, Synthesis and identification of novel pyridazinylpyrazolone based diazo compounds as inhibitors of human islet amyloid polypeptide aggregation, Bioorg. Chem. 84 (2019) 339–346, https://doi.org/10.1016/j.bioorg.2018.11.039.

[26] F. Fraschini, G. Demartini, D. Esposti, Pharmacology of Silymarin, Clin. Drug Investigat. 22 (2002) 51–65, https://doi.org/10.2165/00044011-200222010-00007.
[27] V. Soleimani, P.S. Delghandi, S.A. Moallem, G. Karimi, Safety and toxicity of silymarin, the major constituent of milk thistle extract: an updated review, Phytother. Res. 33 (2019) 1627–1638, https://doi.org/10.1002/ptr.6361.
[28] C. Chu, D. Li, S. Zhang, T. Ikejima, Y. Jia, D. Wang, F. Xu, Role of silibinin in the management of diabetes mellitus and its complications, Arch. Pharm. Res. 41 (2018) 785–796, https://doi.org/10.1007/s12272-018-1047-x.
[29] Y. Wang, Y. Lv, L. Jin, G. Liang, Revealing the mechanism of EGCG, genistein, rutin, quercetin, and silibinin against hIAPP aggregation via computational simulations, Interdiscip. Sci. 12 (2020) 59–68, https://doi.org/10.1007/s12539-019-00352-9.
[30] J. Yang, Y. Sun, F. Xu, W. Liu, Y. Mai, T. Hayashi, S. Hattori, Y. Ushiki-Kaku, S. Onodera, S. Tashiro, T. Ikejima, Silibinin ameliorates amylin-induced pancreatic β-cell apoptosis partly via upregulation of GLP-1R/PKA pathway, Mol. Cell. Biochem. 452 (2019) 83–94, https://doi.org/10.1007/s11010-018-3414-9.
[31] G. Di Fabio, V. Romanucci, C. Di Marino, L. De Napoli, A. Zarrelli, A rapid and simple chromatographic separation of diastereomers of silibinin and their oxidation to produce 2,3-dehydrosilybin enantiomers in an optically pure form, Planta Med. 79 (2013) 1077–1080, https://doi.org/10.1055/s-0032-1328703.
[32] D. Biedermann, E. Vavríková, L. Cvakb, V. Kren, Chemistry of silybin, Nat. Prod. Rep. 31 (2014) 1138–1157, https://doi.org/10.1039/C3NP70122K.
[33] T.-C. Bai, J.-J. Zhu, J. Hu, H.-L. Zhang, C.-G. Huang, Solubility of silybin in aqueous hydrochloric acid solution, Fluid Phase Equilib. 254 (2007) 204–210, https://doi.org/10.1016/j.fluid.2007.03.009.
[34] N. Shigihara, A. Fukunaka, A. Hara, K. Komiya, A. Honda, T. Uchida, H. Abe, Y. Toyofuku, M. Tamaki, T. Ogihara, T. Miyatsuka, H.J. Hiddinga, S. Sakagashira, M. Koike, Y. Uchiyama, T. Yoshimori, N.L. Eberhardt, Y. Fujitani, H. Watada, Human IAPP–induced pancreatic β cell toxicity and its regulation by autophagy, J. Clin. Invest. 124 (2014) 3634–3644, https://doi.org/10.1172/JCI69866.
[35] Y. Kiriyama, H. Nochi, Role and cytotoxicity of amylin and protection of pancreatic islet β-cells from amylin cytotoxicity, Cells 7 (2018) 95, https://doi.org/10.3390/cells7080095.
[36] G. Di Natale, G. Pappalardo, D. Milardi, M.F.M. Sciacca, F. Attanasio, D. La Mendola, E. Rizzarelli, Membrane interactions and conformational preferences of human and avian prion N-terminal tandem repeats: the role of copper(II) ions, pH, and membrane mimicking environments, J. Phys. Chem. B 114 (2010) 13830–13838, https://doi.org/10.1021/jp1033036.
[37] A.A. Adzhubei, M.J.E. Sternberg, A.A. Makarov, Polyproline-II helix in proteins: structure and function, J. Mol. Biol. 425 (2013) 2100–2132, https://doi.org/10.1016/j.jmb.2013.03.018.
[38] N. Blochliger, A. Vitalis, A. Caflisch, High-resolution visualisation of the states and pathways sampled in molecular dynamics simulations, Sci. Rep. 4 (2014) 6264, https://doi.org/10.1038/srep06264.
[39] H. Shoval, D. Lichtenberg, E. Gazit, The molecular mechanisms of the anti-amyloid effects of phenols, Amyloid 14 (2007) 73–87, https://doi.org/10.1080/13506120601116674.
[40] S.A. Gargari, A. Barzegar, A. Tarinejad, The role of phenolic OH groups of flavonoid compounds with H-bond formation ability to suppress amyloid mature fibrils by destabilizing β-sheet conformation of monomeric Aβ17-42, PLoS One 13 (2018), e0199541, https://doi.org/10.1371/journal.pone.0199541.
[41] Afsaneh Porzoor, Benjamin Alford, Helmut M. Hügel, Danilla Grando, Joanne Caine, Ian Macreadie, Anti-amyloidogenic properties of some phenolic compounds, Biomolecules 5 (2015) 505–527, https://doi.org/10.3390/biom5020505.
[42] P.O. Osadebe, E.U. Odoh, P.F. Uzor, Natural products as potential sources of antidiabetic drugs, J. Pharm. Res. Int. (2014) 2075–2095, https://doi.org/10.9734/BJPR/2014/8382.
[43] A.L. Harvey, Natural products in drug discovery, Drug Discov. Today 13 (2008) 894–901, https://doi.org/10.1016/j.drudis.2008.07.004.
[44] A. Pithadia, J.R. Brender, C.A. Fierke, A. Ramamoorthy, Inhibition of IAPP aggregation and toxicity by natural products and derivatives, J. Diabet. Res. 2016 (2015), 2046327, https://doi.org/10.1155/2016/2046327.
[45] P. Velander, L. Wu, F. Henderson, S. Zhang, D.R. Bevan, B. Xu, Natural product-based amyloid inhibitors, Biochem. Pharmacol. 139 (2017) 40–55, https://doi.org/10.1016/j.bcp.2017.04.004.
[46] M.F.M. Sciacca, V. Romanucci, A. Zarrelli, I. Monaco, F. Lolicato, N. Spinella, C. Galati, G. Grasso, L. D'Urso, M. Romeo, L. Diomede, M. Salmona, C. Bongiorno, G. Di Fabio, C. La Rosa, D. Milardi, Inhibition of abeta amyloid growth and toxicity by Silybins: the crucial role of stereochemistry, ACS Chem. Neurosci. 8 (2017) 1767–1778, https://doi.org/10.1021/acschemneuro.7b00110.
[47] S. García-Viñuales, R. Ahmed, M.F.M. Sciacca, V. Lanza, M.L. Giuffrida, S. Zimbone, V. Romanucci, A. Zarrelli, C. Bongiorno, N. Spinella, C. Galati, G. Di Fabio, G. Melacini, D. Milardi, Trehalose conjugates of silybin as prodrugs for targeting toxic Aβ aggregates, ACS Chem. Neurosci. 11 (2020) 2566–2576, https://doi.org/10.1021/acschemneuro.0c00232.
[48] X. Chen, X. Deng, X. Han, Y. Liang, Z. Meng, R. Liu, W. Su, H. Zhu, T. Fu, Inhibition of lysozyme amyloid fibrillation by silybin diastereoisomers: the effects of stereochemistry, ACS Omega 6 (2021) 3307–3318, https://doi.org/10.1021/acsomega.0c05788.
[49] S. Kumar, M.A. Brown, A. Nath, A.D. Miranker, Folded small molecule manipulation of islet amyloid polypeptide, Chem. Biol. 21 (2014) 775–781.
[50] S. Kumar, M. Birol, D.E. Schlamadinger, S.P. Wojcik, E. Rhoades, A.D. Miranker, Foldamer-mediated manipulation of a pre-amyloid toxin, Nat. Commun. 7 (2016) 1–11.
[51] D.C. Rodriguez Camargo, K. Tripsianes, K. Buday, A. Franko, C. Göbl, C. Hartlmüller, R. Sarkar, M. Aichler, G. Mettenleiter, M. Schulz, A. Böddrich, C. Erck, H. Martens, A.K. Walch, T. Madl, E.E. Wanker, M. Conrad, M.H. Angelis, B. Reif, The redox environment triggers conformational changes and aggregation of hIAPP in Type II Diabetes, Sci. Rep. 7 (2017) 44041.
[52] X. Dong, Q. Qiao, Z. Qian, G. Wei, Recent computational studies of membrane interaction and disruption of human islet amyloid polypeptide: monomers, oligomers and protofibrils, Biochim. Biophys. Acta 1860 (2018) 1826–1839, https://doi.org/10.1016/j.bbamem.2018.03.006.
[53] F. Scollo, C. Tempra, F. Lolicato, M.F. Sciacca, A. Raudino, D. Milardi, C. La Rosa, Phospholipids critical micellar concentrations trigger different mechanisms of intrinsically disordered proteins interaction with model membranes, J. Phys. Chem. 9 (2018) 5125–5129.
[54] M.F. Sciacca, F. Lolicato, C. Tempra, F. Scollo, B.R. Sahoo, M.D. Watson, S. García-Viñuales, D. Milardi, A. Raudino, J.C. Lee, A. Ramamoorthy, C. La Rosa, Lipid-chaperone hypothesis: a common molecular mechanism of membrane disruption by intrinsically disordered proteins, ACS Chem. Neurosci. 11 (2020) 4336–4350, https://doi.org/10.1021/acschemneuro.0c00588.
[55] Z. Ridgway, K.-H. Lee, A. Zhyvoloup, A. Wong, C. Eldrid, E. Hannaberry, K. Thalassinos, A. Abedini, D.P. Raleigh, Analysis of baboon IAPP provides insight into amyloidogenicity and cytotoxicity of human IAPP, Biophys. J. 118 (2020) 1142–1151.
[56] K.-H. Lee, D. Noh, A. Zhyvoloup, D. Raleigh, Analysis of prairie vole amylin reveals the importance of the N-terminus and residue 22 in amyloidogenicity and cytotoxicity, Biochemistry 59 (2020) 471–478.
[57] A.Z. Kyung-Hoon Lee, D. Raleigh, Amyloidogenicity and cytotoxicity of des-Lys-1 human amylin provides insight into amylin self-assembly and highlights the difficulties of defining amyloidogenicity, Protein Eng. Design Select. 32 (2019) 87–93.
[58] D. Milardi, M.F.M. Sciacca, M. Pappalardo, D.M. Grasso, C. La Rosa, The role of aromatic side-chains in amyloid growth and membrane interaction of the islet amyloid polypeptide fragment LANFLVH, Eur. Biophys. J. 40 (2011) 1–12.
[59] T. Doran, A. Kamens, N. Byrnes, B. Nilsson, Role of amino acid hydrophobicity, aromaticity, and molecular volume on IAPP(20-29) amyloid self-assembly, Proteins 80 (2012) 1053–1065.
[60] R. Azriel, E. Gazit, Analysis of the minimal amyloid-forming fragment of the islet amyloid polypeptide an experimental support for the key role of the phenylalanine residue in amyloid formation, J. Biol. Chem. 276 (2001) 34156–34161.
[61] L.-H. Tu, D.P. Raleigh, Role of aromatic interactions in amyloid formation by islet amyloid polypeptide, Biochemistry 52 (2013) 333–342.
[62] P. Marek, A. Abedini, B. Song, M. Kanungo, M.E. Johnson, R. Gupta, W. Zaman, S. S. Wong, D.P. Raleigh, Aromatic interactions are not required for amyloid fibril formation by islet amyloid polypeptide but do influence the rate of fibril formation and fibril morphology, Biochemistry 46 (2007) 3255–3261.
[63] C. Betsholtz, L. Christmanson, U. Engström, F. Rorsman, K. Jordan, T.D. O'Brien, Structure of cat islet amyloid polypeptide and identification of amino acid residues of potential significance for islet amyloid formation, Diabetes 39 (1990) 118–122.
[64] S. Jha, J.M. Snell, S.R. Sheftic, S.M. Patil, S.B. Daniels, F.W. Kolling, A. T. Alexandrescu, pH dependence of amylin fibrillization, Biochemistry 53 (2014) 300–310.
[65] P.T. Nguyen, X. Zottig, M. Sebastiao, S. Bourgault, Role of site-specific asparagine deamidation in islet amyloid polypeptide amyloidogenesis: key contributions of residues 14 and 21, Biochemistry 56 (2017) 3808–3817.
[66] E. Godin, P. Nguyen, X. Zottig, S. Bourgault, Identification of a hinge residue controlling islet amyloid polypeptide self-assembly and cytotoxicity, J. Biol. Chem. 294 (2019) 8452–8463.
[67] Y.P.Y. Lam, C.A. Wootton, I. Hands-Portman, J. Wei, C.K.C. Chiu, I. Romero-Canelon, F. Lermyte, M.P. Barrow, P.B. O'Connor, Does deamidation of islet amyloid polypeptide accelerate amyloid fibril formation? Chem. Commun. 54 (2018) 13853–13856.
[68] E.B. Dunkelberger, L.E. Buchanan, P. Marek, P. Cao, D.P. Raleigh, M.T. Zanni, Deamidation accelerates amyloid formation and alters amylin fiber structure, J. Am. Chem. Soc. 134 (2012) 12658–12667.
[69] M.R. Nilsson, M. Driscoll, D.P. Raleigh, Low levels of asparagine deamidation can have a dramatic effect on aggregation of amyloidogenic peptides: implications for the study of amyloid formation, Protein Sci. 11 (2002) 342–349.
[70] M.F. Sciacca, V. Romanucci, A. Zarrelli, I. Monaco, F. Lolicato, N. Spinella, C. Galati, G. Grasso, L. D'Urso, M. Romeo, Inhibition of Aβ amyloid growth and toxicity by silybins: the crucial role of stereochemistry, ACS Chem. Neurosci. 8 (2017) 1767–1778.
[71] K. Vanommeslaeghe, E.P. Raman, A.D. MacKerell, Automation of the CHARMM General Force Field (CGenFF) II: assignment of bonded parameters and partial atomic charges, J. Chem. Inf. Model. 52 (2012) 3155–3168, https://doi.org/10.1021/ci3003649.
[72] K. Vanommeslaeghe, A.D. MacKerell, Automation of the CHARMM General Force Field (CGenFF) I: bond perception and atom typing, J. Chem. Inf. Model. 52 (2012) 3144–3154, https://doi.org/10.1021/ci300363c.
[73] H.J.C. Berendsen, D. van der Spoel, R. van Drunen, GROMACS: a message-passing parallel molecular dynamics implementation, Comput. Phys. Commun. 91 (1995) 43–56, https://doi.org/10.1016/0010-4655(95)00042-E.
[74] J. Huang, S. Rauscher, G. Nawrocki, T. Ran, M. Feig, B.L. de Groot, H. Grubmüller, A.D. MacKerell, CHARMM36m: an improved force field for folded and intrinsically disordered proteins, Nat. Methods 14 (2017) 71–73, https://doi.org/10.1038/nmeth.4067.

[75] W.L. Jorgensen, J. Chandrasekhar, J.D. Madura, R.W. Impey, M.L. Klein, Comparison of simple potential functions for simulating liquid water, J. Chem. Phys. 79 (1983) 926–935, https://doi.org/10.1063/1.445869.
[76] G. Bussi, D. Donadio, M. Parrinello, Canonical sampling through velocity rescaling, J. Chem. Phys. 126 (2007), 014101, https://doi.org/10.1063/1.2408420.
[77] H.J.C. Berendsen, J.P.M. Postma, W.F. van Gunsteren, A. DiNola, J.R. Haak, Molecular dynamics with coupling to an external bath, J. Chem. Phys. 81 (1984) 3684–3690, https://doi.org/10.1063/1.448118.